Hindawi
Shock and Vibration
Volume 2023, Article ID 5795266, 9 pages
https://doi.org/10.1155/2023/5795266

Research Article

The Influence of the Load Type on the Center Frequency Tuning of the Variable-Flux Biaxial Energy Harvester

Karim El-Rayes, Salam Gabran, and William Melek

Department of Mechanical and Mechatronics Engineering, University of Waterloo, Waterloo, Canada

Correspondence should be addressed to Karim El-Rayes; kelrayes@uwaterloo.ca

Received 14 November 2022; Revised 8 January 2023; Accepted 31 January 2023; Published 15 February 2023

Academic Editor: Jiaxi Zhou

The variable-flux biaxial energy harvester (VBH) is a novel vibration energy harvester (VEH) architecture in which a ferromagnetic mass moves against an assembly of a coil and a stationary permanent magnet. The varying flux lines induce potential differences across the coil terminals. Unlike conventional VEHs, the center frequency of the VBH can be tuned by mechanical, electronic, or electromagnetic mechanisms to maximize the generated power. In this research, we demonstrate the impact of two types of loads, purely resistive and complex RC loads, on the harvester center frequency. We also demonstrate a mechanism that utilizes RC load to tune the center frequency of the VBH. In comparison to conventional purely resistive loads, the introduced capacitive load allows control of the total VBH stiffness and, accordingly, modulates the center frequency and eliminates the need for mechanical pretuning of the VBH center frequency.

1. Introduction

The variable-flux biaxial energy harvester (VBH) is a device that can capture and convert kinetic energy from low-frequency vibrations into useable electric energy [1, 2]. This is achieved through a unique transduction mechanism that involves disrupting a stationary magnetic field with a moving ferromagnetic object, which generates an electromotive force (EMF) across a stationary coil in the vicinity of the field. Low-frequency vibrations, which occur naturally and are a significant source of kinetic energy, can be found in a range of sources, including mechanical vibrations (0.6–2.5 Hz) [3], human motion (0.6–5 Hz) [4], and vehicle bouncing (1–10 Hz) [5]. However, harvesting kinetic energy from low-frequency vibrations can be challenging due to the need for large proof masses and a decrease in harvesting bandwidth below 10 Hz. The variable-flux biaxial energy harvester (VBH) is capable of effectively harvesting low-frequency vibrations using a small proof mass of only 9.8 grams as demonstrated in Figure 1 and 2. In addition to this, the center frequency of the VBH can be tuned mechanically, magnetically, or electronically. However, the first two methods can be complex and require human intervention, which may be difficult in inaccessible environments and can be costly. In contrast, electronic tuning is simpler, requiring fewer electronic components, and can be automated to reduce the need for manual tuning. It is also more cost-effective compared to the other methods [6–9].

The VBH is composed of an impact oscillator connected to an inductive circuit. The oscillator consists of a steel sphere and mechanical end springs. The inductive circuit includes a top magnet, a coil, and a moving steel sphere. The top magnet is the source of the magnetic force, and the coil is wound around a dielectric tube with a single magnet placed on top. The ferromagnetic sphere can move freely along a track inside the tube, and the VBH's peak frequency is adjusted through the use of two springs attached to the end caps of the tube. The VBH is mounted on an electrically nonconductive material with the center lines of the magnet and coil aligned with the track's midsection. The specifications of the VBH are listed in Table 1.

To provide context, the VBH relies on two types of restoring forces: a magnetic force from a permanent magnet and a mechanical force from compression springs mounted on the ends of the travel track. The magnetic restoring force F_m, which is the primary restoring force component, is a

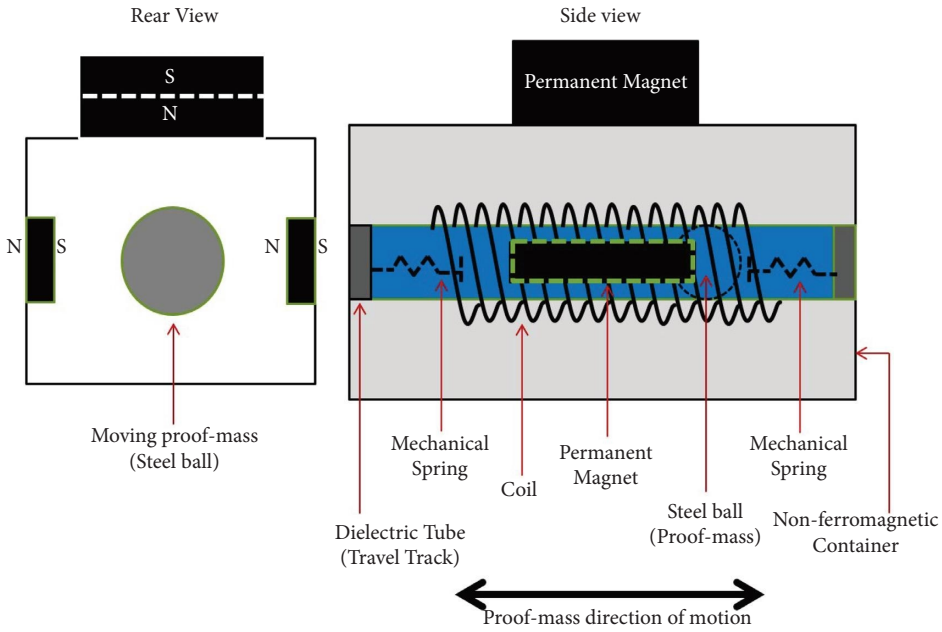

Figure 1: Side and end views of the VBH (not to scale).

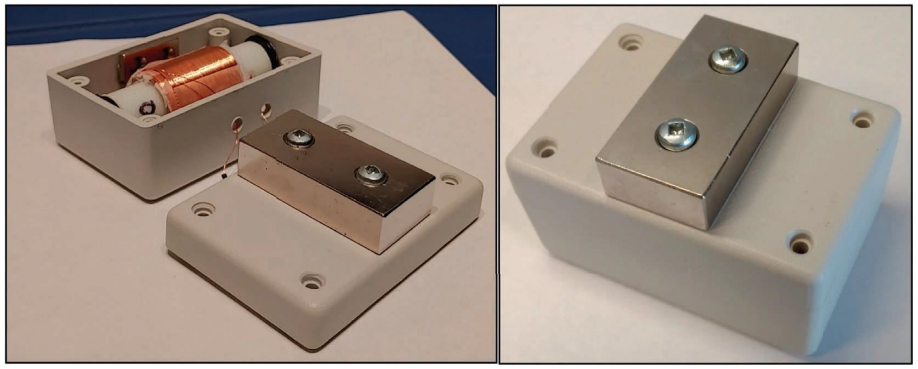

Figure 2: Variable-flux biaxial energy harvester internals (a) and exteriors (b).

function of the magnetic field characteristics (residual flux density and demagnetization force) and the distance between the permanent magnet and the steel ball. The system was simulated using QuickField FEA software [12], and the results shown in Figures 3 and 4 demonstrate the variation in the magnetic flux density B, magnetic field intensity H, and force exerted on the steel ball as shown in Table 2. With the position of the steel ball along the travel track, the VBH output voltage waveform is shown in Figure 5. This causes the permanent magnet to act like a virtual decompression spring, leading to the use of the term "magnetic restoring force" as a synonym for a mechanical spring restoring force. The mathematical model for the VBH is [2]

$$\ddot{x} + \left(\frac{c_m + c_e}{m}\right)\dot{x} + \left(\frac{c_3}{m}\right)x^2\dot{x} + \left(\frac{F_s}{m}\right) + \frac{1}{m}\left(-5.19x^3 - 23.05x^2 + 14.28x + 2.92\right) = \ddot{y}(t), \quad (1)$$

Table 1: VBH mechanical and electrical specifications.

Parameters	Value
Travel track total length (mm)	72
Unstretched end-spring length (mm)	14.5
Compressed end-spring length (mm)	13.5
End-spring inner diameter (mm)	8.9
End-spring outer diameter (mm)	10.75
Stainless steel ball diameter (mm)	13.05
Stainless steel ball mass (grams)	8.9
Proof-mass travel distance (mm)	30
Distance between top magnet and coil (mm)	14
Distance between side magnets (mm)	26.3
Coil inductance (μH)	3.4
Coil resistance (Ω)	10.6
Coil number of turns	970
Top magnet part number [10]	BY0X08DCS
Side magnets' part number [11]	BX082CS-S

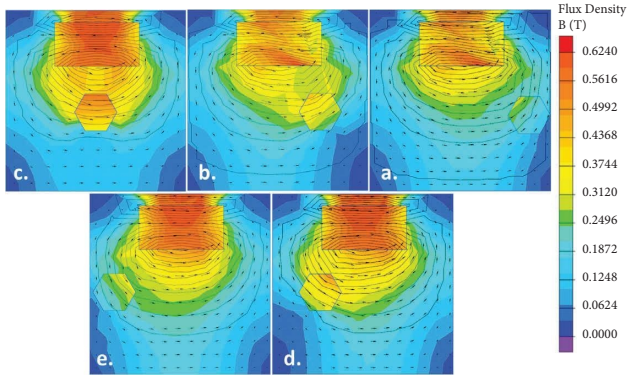

Figure 3: Magnetic flux density B distribution for different locations of the moving object simulated with QuickField.

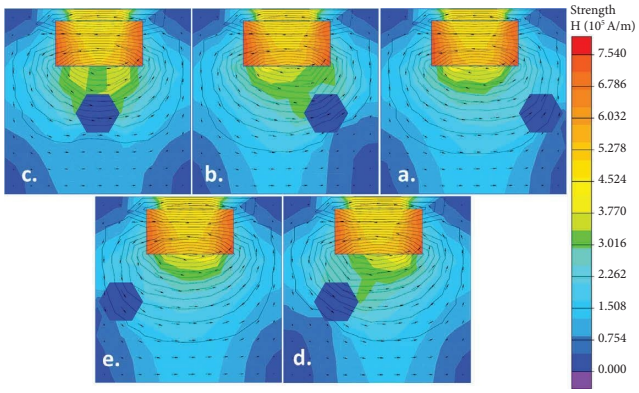

Figure 4: Magnetic field intensity H distribution for different locations of the moving object simulated with QuickField.

where $\ddot{x}$ and $\dot{x}$ represent the acceleration and velocity of the proof mass, respectively, while c_m and c_e are the mechanical and electrical damping coefficients, c_3 is the cubic damping coefficient resulting from impact losses, m is the mass of the moving object (in this case, a metallic ball), F_s is the mechanical spring's restoring force, and $\ddot{y}(t)$ is the external excitation. The term $(1/m)(-5.19x^3 - 23.05x^2 + 14.28x + 2.92)$ represents the magnetic restoring force, F_m, exerted by the permanent magnet on the moving ferromagnetic object (a steel ball in the experimental setup). A detailed analysis and derivation of the magnetic restoring force for the variable-flux biaxial energy harvester (VBH) can be found in [2].

The output power generated by the VBH at resonance can range from 0.11 to 127.16 μW, depending on the values of the attached RC load. This is sufficient to power, low-power microcontrollers, such as the nanoWatt XLP eXtreme low power PIC microcontrollers family from Microchip Technology [13–15], the STM8L/STM8AL [16], and STM32L [17] microcontroller families from STMicroelectronics. While the amount of power generated by the VBH may be considered low, it is sufficient to power ultralow-power wireless communication modules and protocols such as EnOcean STM300 [18], SX1262, RFM95, inAir9 [19], Zigbee, and Thread [20], which only require a few tens of microWatts.

Table 2: Mechanical force applied on the moving steel ball at different locations simulated with QuickField.

Steel ball location	Force (N)
Position a	−7.93
Position b	−13.46
Position c	7.31
Position d	11.7
Position e	6.8

2. Experimental Results

Experiments conducted on earlier prototypes of the VBH [1] with purely capacitive loads showed a significantly different voltage-frequency response in comparison with purely resistive loads and open-loop operation, in which no loads were connected to the output. The observed change in the center frequency established grounds to test the VBH with an in-series resistor-capacitor complex load structure to study the effect of added stiffness and damping to the system due to the load resistance and capacitance and how the load can be used to tune the center frequency without any mechanical or magnetic pretuning such as changing the proof mass or the magnetic field intensity [6, 7]. The experimental setup to test the VBH with in-series RC load is shown in Figures 6 and 7. A basic demonstration setup, shown in Figure 8, was used to visually demonstrate the generated power using a low-power light emitting diode (LED) and a 1 : 10 step-up transformer.

All experiments were conducted in the frequency range of 5–25 Hz at a sweep rate of 5 Hz/ min and amplitude of 0.9 g (1 $g = 9.81\ m/s^2$) to mimic the amplitude of human walking. It is worth noting that every experiment was conducted multiple times to ensure the validity and reproducibility of the results.

Experimental results exhibited that using a load consisting of in-series resistor-capacitor pair with the output of the VBH, as shown in in Figure 9, affects the center frequency, which is a result of increased stiffness introduced by the capacitance component of the load, to the VBH system. Figure 10 and Table 3 demonstrate the measured voltage-frequency response and center frequency of the VBH for different in-series RC loads, respectively. The governing equation for the center frequency as a function of stiffness and damping for a mass on spring oscillator is [21]

$$\omega_n = \sqrt{\frac{k}{m}}, \tag{2}$$

and [21]

$$\eta = \frac{B_m Z_L + (Bl)^2}{2Z_L\sqrt{mk}} = \frac{B_m}{2\omega_n m} + \frac{Bl^2/Z_L}{2\omega_n m} = \eta_m + \eta_e, \tag{3}$$

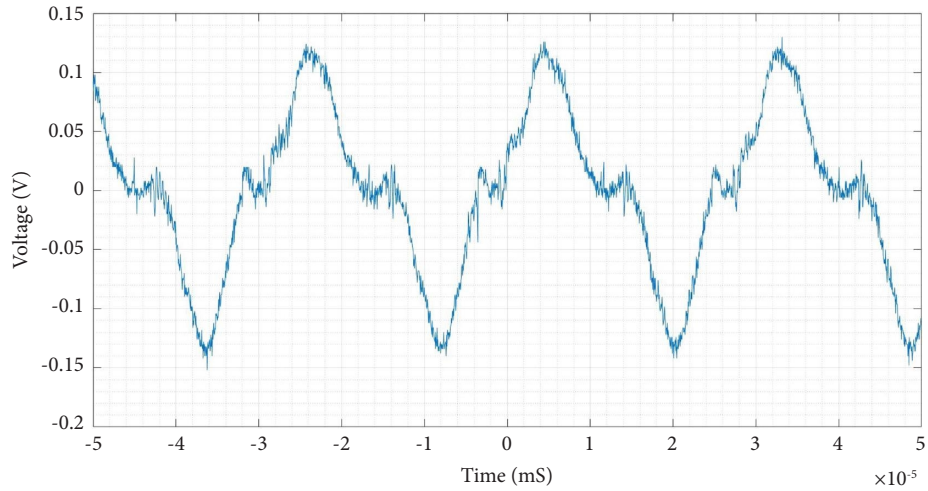

Figure 5: VBH output voltage waveform.

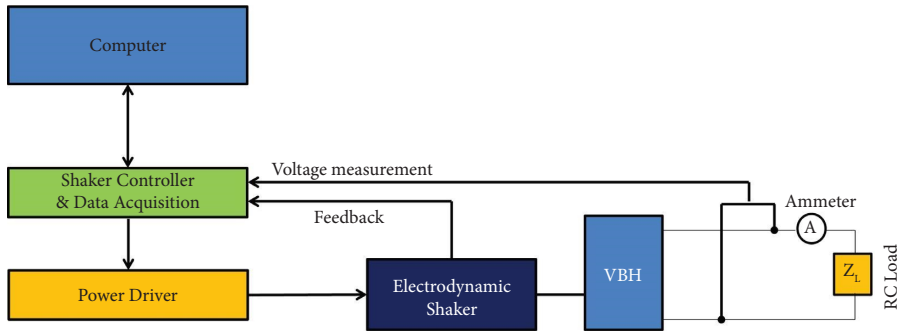

Figure 6: A schematic of the experimental setup of the VBH with in-series RC load.

where ω_n is the natural frequency, k is the total stiffness of the oscillator, and m is the proof-mass of the moving object, η, η_m, and η_e are the total, mechanical, and electrical damping factors, respectively, B_m is the energy extraction damping factor, B is the magnetic flux density, l is the coil length, and $|Z_L|$ is the magnitude of load impedance. For a complex RC load, the magnitude is

$$|Z_L| = \sqrt{R_L^2 + |X_c|^2}, \tag{4}$$

where R_L is the resistive component and $|X_c|$ is the magnitude of the capacitive reactance component of the load impedance, where the capacitive reactance is a function of capacitance and generated EMF frequency:

$$\begin{aligned} X_c &= \frac{1}{\omega_c C} \\ &= \frac{1}{2\pi f_c C}, \end{aligned} \tag{5}$$

where ω is the center angular frequency of the voltage across the capacitor, which can be substituted with the term $2\pi f_c$, f_c is the center frequency in Hertz, and C is the capacitance in Farad. Experiments conducted with purely resistive and complex RC loads (as listed in Tables 4 and 3) demonstrated

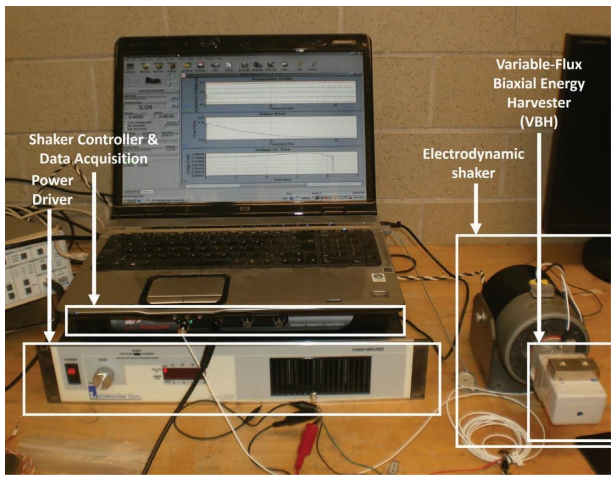

Figure 7: The experimental setup of the VBH.

that the center frequency changed, indicating a change in system stiffness k. The proof mass was kept constant across all experiments to emphasize that the change in center frequency was due solely to the change in the system's stiffness. To further validate this observation, the VBH was tested with complex loads of different capacitance values,

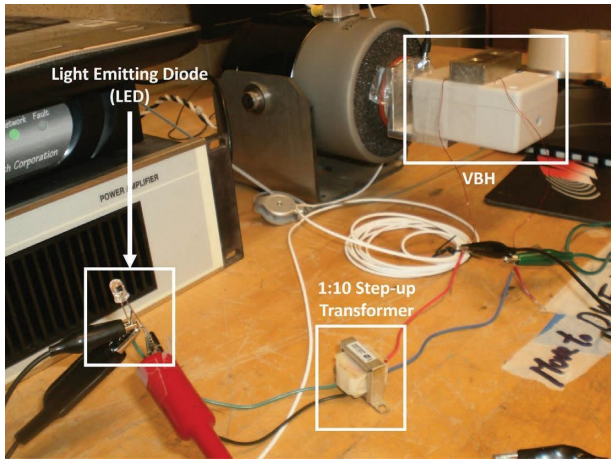

Figure 8: A simple demonstrator using the VBH with a step-up transformer and light emitting diode (LED).

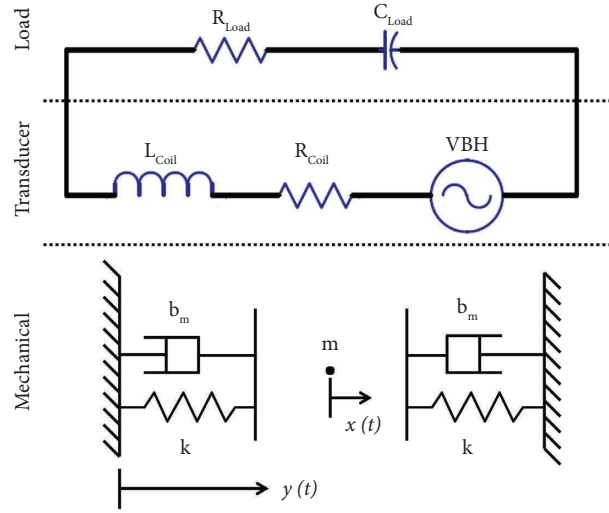

Figure 9: Representation of the variable-flux biaxial energy harvester, VBH, with complex RC load impedance, where L_{coil}, R_{coil}, R_{Load}, C_{Load}, m, k, and b_m are the harvester's coil inductance, coil resistance, load resistance, load capacitance, moving proof-mass, mechanical stiffness, and mechanical damping, respectively.

while keeping the value of the resistive component unchanged. Results showed a variation in the center frequency of 0.33 Hz for capacitance values between 10 and 25100 μF. Furthermore, comparing test results conducted with a purely resistive load with tests conducted with in-series RC load that uses the same resistance value, the center frequency has dropped by 0.4–0.65 Hz when capacitance is added, indicating a reduction in system stiffness k. Experimental results for RC load and purely resistive load versus center frequency are shown in Tables 3 and 4, respectively.

To test the VBH in a real-world scenario where DC output power, and not AC, is required to power up different electronic devices, the VBH output was connected to a step-up transformer with a primary-to-secondary coil turns ratio of 1 : 10, followed by a Schottky-based full-wave rectifier and ripple filtering capacitor to provide a complete power unit design. This power unit design is meant to resolve two main challenges:

(i) Output voltage amplitude is too low for most electronic devices to operate on

(ii) Generic silicon diode-based full-wave rectifiers cannot rectify AC signals smaller than 700–800 mV

A Schottky diode-based full-wave rectifier was used for its low forward voltage (150–450 mV) compared to generic silicon diode rectifiers, and the ripple filter capacitor at the output stage is added to smooth the output signal and eliminate ripples. A schematic of the power unit is shown in Figure 11.

Experiments showed that the filter capacitor adds extra stiffness to the system resulting in a higher center frequency f_c with the increase of the capacitance value. This confirms the previously discussed conclusion of the directly proportional effect of output capacitance on the VBH's total stiffness. Figures 12 and 13 show the V-F response of the power unit for a frequency sweep 5–25 Hz at 0.9 g excitation; a comparison of different filter capacitor values versus center frequency is shown in Table 5. The hysteresis in $V - F$ response might catch the attention of the reader; an early conclusion explains such hysteresis is due to additional nonlinear components to the output load network represented by the step-up transformer and Schottky diode full-wave rectifier; however, it is not of interest in the scope of this article.

2.1. Discussion. The complex RC load adds extra damping and stiffness to the system; however, the added damping and stiffness are not of the same magnitude. Experimental results in Table 3 show that the added damping due to the resistive component of the load, represented by 3dB bandwidth as a measure, is qualitatively small, ranging only between 2.51 and 2.72 Hz for tested values included in the experimental results, even when the resistive component is multiple folds of the VBH parasitic resistance, $R_c$oil, where Q is the quality factor and ζ is the damping ratio. On the contrary, the complex load's capacitive component increases the compliance of the system (compliance is the reciprocal of stiffness), resulting in a change in the VBH total stiffness that ranged between 23.128 and 26.25 for the different complex load values included in the experimental data, which consequently resulted in a change in center frequency, f_c, between 8.07 Hz and 8.64 Hz which is close to 7% when compared to the open-loop center frequency. In conclusion, the complex load RC components can be selected to tune the center frequency to a selected value or range to maximize energy harvesting and power transfer without a significant impact on the harvesting bandwidth.

2.2. Power Analysis for RC Load. The power generated in magnetic-induction generator through sinusoidal excitation is given by [21]

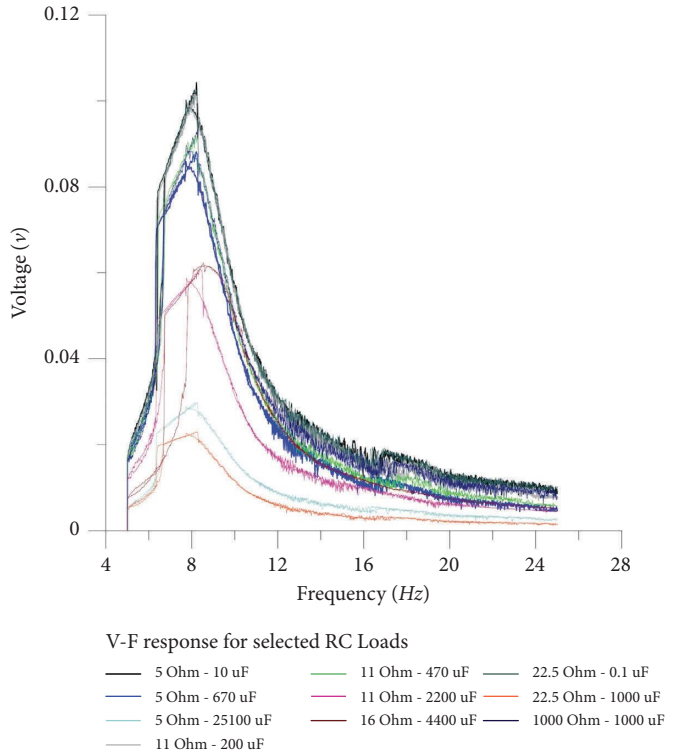

Figure 10: Measured voltage-frequency response for selected RC load values at an excitation of $A_o = 0.9g$.

Table 3: VBH center frequency for different RC network loads.

Resistance (Ω)	Capacitance (μF)	Center frequency (Hz)	Maximum voltage (mV)	RMS current (mA)	Resistive power ($S = I^2X_c)\mu VA$	Real power ($P = I^2R)\mu W$	Bandwidth (Hz)	Total stiffness ($k = \omega^2 m$)	Power density (W/m^3)
5	10	8.2	104.3	0.18	62.86	0.16	2.62	23.644	0.00081
5	100	8.22	102.8	0.627	76.09	1.97	2.72	23.760	0.009828225
5	670	8.2	88.2	2.5	180.98	31.25	2.55	23.644	0.15625
5	820	8.45	84.7	3.1	220.65	48.05	2.51	25.108	0.24025
5	1000	8.23	79.8	3	173.98	45.00	2.52	23.818	0.225
5	1200	8.15	73.7	3.2	166.57	51.20	2.54	23.357	0.256
5	7700	8.45	34.39	4.6	51.74	105.80	2.65	25.108	0.529
5	25100	8.11	29.8	4	12.50	80.00	2.67	23.128	0.4
8.4	1000	8.44	81.1	2.8	147.78	65.86	2.52	25.049	0.32928
11	200	8.2	101.24	1	97.01	11.00	2.66	23.644	0.055
11	470	8.23	91.96	1.8	133.26	35.64	2.57	23.818	0.1782
11	680	8.23	84.41	2.3	150.38	58.19	2.57	23.818	0.29095
11	820	8.47	81.42	2.6	154.84	74.36	2.51	25.227	0.3718
11	1000	8.2	77.57	2.6	131.15	74.36	2.51	23.644	0.3718
11	2200	8.4	60.89	3.2	88.15	112.64	2.53	24.812	0.5632
11	3100	8.4	55.84	3.3	66.53	119.79	2.54	24.812	0.59895
11	4400	8.64	52.5	3.4	48.38	127.16	2.646	26.250	0.6358
11	5400	8.46	52.09	3.4	40.26	127.16	2.61	25.167	0.6358
11	22000	8.72	50	3.4	9.59	127.16	2.59	26.738	0.6358
15	100	8.15	86.79	0.37	26.72	2.05	2.57	23.357	0.0102675
16	2200	8.54	60.69	2.7	61.73	116.64	2.6	25.646	0.5832
16	4400	8.52	62.29	2.8	33.27	125.44	2.55	25.526	0.6272
16	22000	8.54	60.69	2.8	6.64	125.44	2.59	25.646	0.6272

Table 3: Continued.

Resistance (Ω)	Capacitance (μF)	Center frequency (Hz)	Maximum voltage (mV)	RMS current (mA)	Resistive power ($S = I^2X_c)\mu VA$	Real power ($P = I^2R)\mu W$	Bandwidth (Hz)	Total stiffness ($k = \omega^2 m$)	Power density (W/m^3)
22.5	0.1	8.23	102.41	0.0022	0.94	0.00	2.69	23.818	5.445E−07
22.5	10	8.18	103.36	0.071	9.80	0.11	2.66	23.529	0.000567113
22.5	100	8.21	85.59	0.355	24.42	2.84	2.57	23.702	0.014177813
22.5	1000	8.25	23.07	0.564	6.13	7.16	2.55	23.934	0.0357858
100	10	8.23	101.8	0.065	8.17	0.42	2.66	23.818	0.0021125
100	1000	8.07	48.7	0.365	2.63	13.32	2.66	22.901	0.0666125
1000	10	8.14	100.7	0.04	3.13	1.60	2.67	23.300	0.008
1000	1000	8.25	93.5	0.07	0.09	4.90	2.62	23.934	0.0245

Table 4: VBH center frequency for purely resistance loads.

Resistance (Ω)	Center frequency (Hz)
0	8.75
5	8.84
8.6	8.86
22.6	8.81
100	8.83
1000	8.84
2000	8.79
3240	8.84
9000	8.66
Open loop (no load)	8.18

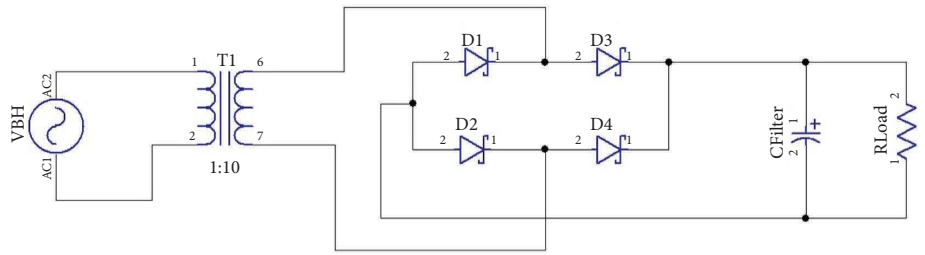

Figure 11: Schematic of a power supply unit using the VBH as a power source.

$$P = \frac{m\eta_e A_o^2 (\omega/\omega_n)^3 \omega^3}{\left[1 - (\omega/\omega_n)^2\right]^2 + \left[2\eta(\omega/\omega_n)\right]^2}, \tag{6}$$

where m is the proof mass of the moving object, A_o^2 is the amplitude of the excitation signal, η and η_e are the total and electrical damping factors, and ω and ω_n are the operating and natural frequencies, respectively. The maximum power is generated; when the operating frequency ω is equal to the natural frequency ω_n, the maximum power will reduce to [21]

$$P_{\max} = \frac{m\eta_e A_o^2 \omega_n^3}{4\eta^2}. \tag{7}$$

For VBH, the power generated across an RC load cannot be calculated directly. Real power (for resistive loads) and reactive power (for capacitive loads) must be calculated separately and then combined to calculate the apparent power S. The generated power formula (7) was cross-validated against experimentally measurements listed in Table 3; measured power was calculated using the following formula:

$$P = I_{\text{rms}}^2 Z, \tag{8}$$

where I_{rms} is the measured RMS current in Ampere and Z is the resistance or capacitive reactance.

The electrical damping factor (η_e) from [21] is modified to calculate the reactive power (for a capacitive load):

$$\eta_e = \frac{Bl^2/X_c}{2\omega_n m}, \tag{9}$$

and for real power (for a resistive load), η_e is modified as well to become

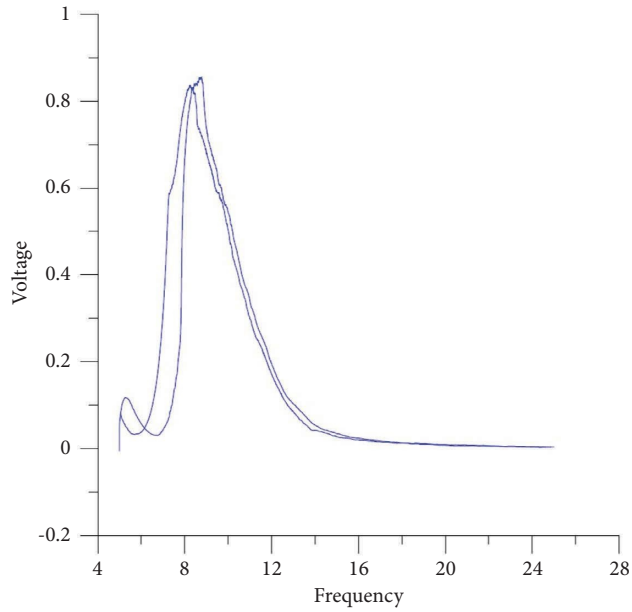

Figure 12: Voltage vs. frequency response of the power supply unit at 100K Ω resistive load and 100 μF filter capacitor.

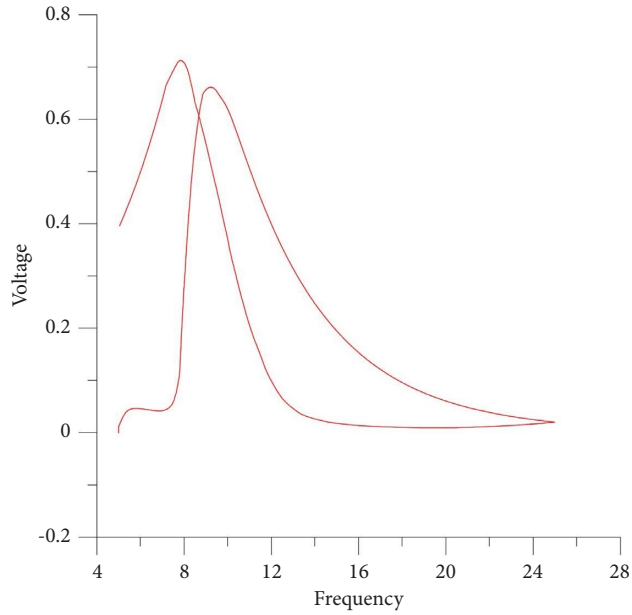

Figure 13: Voltage vs. frequency response of the power supply unit at 100K Ω resistive load and 1000 μF filter capacitor.

Table 5: A center frequency (f_c) comparison for the PSU up and down sweeps using 10, 100, and 1000 μF filter capacitors for 100 Ω resistive load.

Filter capacitor value (μF)	f_c (up sweep) (Hz)	f_c (down sweep) (Hz)	Max voltage in up sweep cycle (mv)	Max voltage in down-sweep cycle (mv)
10	8.52	8.37	907	894
100	8.72	8.17	991	969
1000	9.2	7.83	661	712

$$\eta_e = \frac{Bl^2/R_L}{2\omega_n m}, \tag{10}$$

and apparent power, S, is given by

$$|S| = \sqrt{P^2 + Q^2}, \tag{11}$$

where P is the real power and Q is the reactive power.

3. Conclusion

In this article, we introduce a new mechanism to tune the center frequency of a variable-flux biaxial energy harvester (VBH) using an in-series RC load. Adding a capacitive component in series with the resistive load increases the total system stiffness, resulting in changing the center frequency. The presented mechanism reduces the dependence on mechanical and magnetic pretuning of the VBH, allowing the VBH to retune its center frequency and increase the generated power for any operating frequency. Experimental results for the presented system showed a change in center frequency between 8.19 Hz and 8.72 Hz for selected RC load values.

Data Availability

The data used to support the findings of the study are available within the article.

Conflicts of Interest

The authors declare that they have no conflicts of interest.

References

[1] K. El-Rayes, A. Abdel-Aziz, E. Abdel-Rahman, R. Mansour, and E. El-Saadany, *Prototypes of a Field Disruption Energy Harvester*, ASME IDETC, Chicago, IL, USA, 2012.

[2] K. El-Rayes, S. Gabran, E. Abdel-Rahman, and W. Melek, "Variable-flux biaxial vibration energy harvester," *IEEE Sensors Journal*, vol. 18, no. 8, pp. 3218–3227, 2018.

[3] P. Barralon, N. Noury, and N. Vuillerme, "Classification of daily physical activities from a single kinematic sensor," in *Proceedings of the IEEE Engineering in Medicine and Biology 27th Annual Conference*, pp. 2447–2450, Shanghai, China, September 2005.

[4] A. Godfrey, R. Conway, D. Meagher, and G. Olaighin, "Direct measurement of human movement by accelerometry," *Medical Engineering & Physics*, vol. 30, no. 10, pp. 1364–1386, 2008.

[5] J. Granlund, *Vehicle and Driver Vibrations*, Vectura consulting AB, Stockholm, Sweden, 2010.

[6] J. A. Bowden, S. G. Burrow, A. Cammarano, L. R. Clare, and P. D. Mitcheson, "Switched-Mode load impedance synthesis to parametrically tune electromagnetic vibration energy harvesters," *IEEE*, vol. 20, no. 2, pp. 603–610, 2015.

[7] J. A. Bowden, S. G. Burrow, and L. R. Clare, "Switched-mode impedance synthesis for electrical tuning of a vibration energy harvester," in *Proceedings of the 13th International Conference on Micro and Nanotechnology for Power Generation and Energy Conversion Applications (PowerMEMS 2013)*, London, UK, December 2013.

[8] H. Zhang, L. R. Corr, and T. Ma, "Effects of electrical loads containing non-resistive components on electromagnetic vibration energy harvester performance," *Mechanical Systems and Signal Processing*, vol. 101, pp. 55–66, 2018.

[9] H. Luo, G. Gu, W. Shang et al., "Interactive-excited waterdrop triboelectric nanogenerator with ultrahigh charge density and instantaneous power," *Nano Energy*, vol. 97, Article ID 107158, 2022.

[10] Kjmagnetics, "Neodymium block magnet type BY0X08DCS," 2010, https://www.kjmagnetics.com/proddetail.asp?prod=BY0X08DCS.

[11] Kjmagnetics, "Neodymium block magnet type BX082CS-S," 2010, https://www.kjmagnetics.com/proddetail.asp?prod=BX082CS-S&cat=19.

[12] QuickField, "QuickField finite element analysis software," 2021, https://quickfield.com/.

[13] M. Hofmann, "Technical review: practical applications of low-power design with nanoWatt XLP," 2022, http://ww1.microchip.com/downloads/en/devicedoc/future%20xlp%20article.pdf.

[14] Microchip, "nanoWatt XLP eXtreme Low Power PIC® MCUs," 2022, http://ww1.microchip.com/downloads/en/devicedoc/39941d.pdf.

[15] Microchip, "PIC12F1822/16F182X 8/14/20-pin 8-bit flash microcontroller product datasheet," 2009, https://ww1.microchip.com/downloads/aemDocuments/documents/OTH/ProductDocuments/DataSheets/41406B.pdf.

[16] St Microelectronics, *AN3147: Power Management in STM8L and STM8AL*, ST Microelectronics, Geneva, Switzerland, 2013.

[17] St Microelectronics, *TA0340 Technical Article STM32L Cortex-M3 Microcontroller for Usage in Low-Power Healthcare Applications*, ST Microelectronics, Geneva, Switzerland, 2011.

[18] C. Bach, "Stm 300 thermo or battery powered – power supply alternatives to solar panel," 2020, https://www.enocean.com/wp-content/uploads/application-notes/AN209_STM_Thermo_or_Battery_Powered_Option_2020.pdf.

[19] E. Bäumker, A. Miguel Garcia, and P. Woias, "Minimizing power consumption of LoRa and LoRaWAN for low-power wireless sensor nodes," *Journal of Physics: Conference Series*, vol. 1407, no. 1, Article ID 012092, 2019.

[20] F. Moreno-Cruz, V. Toral-López, A. Escobar-Molero, V. U. Ruíz, A. Rivadeneyra, and D. P. Morales, "treNch: ultra-low power wireless communication protocol for IoT and energy harvesting," *Sensors*, vol. 20, no. 21, p. 6156, 2020.

[21] L. Mateu and F. Moll, "Review of energy harvesting techniques and applications for microelectronics," in *Proceedings of the SPIE 5837 VLSI Circuits and Systems II*, p. 5837, Sevilla, Spain, June 2005.